Energy Proceedings
Vol 55, 2025
ISSN 2004-2965

Flow Structure and Heat Transfer in a Channel With the Streamwise Ribs Arranged in the Buffer Layer#

Jiarui Gong, Jiansheng Wang*, Xueling Liu*, Jintao Niu, Xuqing Wang

School of Mechanical Engineering, Tianjin University, Tianjin, 300354, P. R. China

(Corresponding Author: jsw@tju.edu.cn and lxling@tju.edu.cn)

ABSTRACT

In the present study, the streamwise ribs are arranged in the buffer layer without destroying the viscous sublayer of the turbulent boundary layer in the rectangular channel, which aim to achieve the drag reduction and maintain the heat transfer performance simultaneously. The numerical calculation is carried out at *Re* = 3745, 4745, and 5745. The ribs induce plenty of small-scale secondary vortices in the viscous sublayer and the buffer layer. These vortices can suppress the sweep motions of the high-speed fluid carried by large-scale vortices. The friction loss on the bottom of the channel significantly decreases and the drag reduction efficiency can be up to 26.282% at *Re* = 5745. Meanwhile, the sweeping motion of the fluid between the adjacent ribs destroys the temperature boundary layer and the heat transfer performance is intensified. The excess heat transfer can compensate the local heat loss below the ribs so that the heat transfer performance maintains at the original level at *Re* =3745. The Nusselt number on the bottom even increases at higher *Re*. The maximum comprehensive performance coefficient is up to 1.112.

Keywords: heat transfer, flow control, turbulent flow, drag reduction, streamwise rib

NONMENCLATURE

Abbreviations	
DNS	Direct numerical simulation
LES	Large eddy simulation
Symbols	
C_f	Skin-friction coefficient
C_s	Smargorinsky constant
h	Heat transfer coefficient
H	Half height of the channel
Nu	Nusselt number
Nu_x	Local Nusselt number
p	Pressure
Pr	Prandtl number
q_w	Wall heat flux
Re	Reynold number
S_{ij}	Strain rate tensor
ΔT	Temperature difference
T_{in}	Inlet temperature
T_w	Bottom temperature
T_τ	Wall friction temperature
u, v, w	X, Y, Z velocity component
u_τ	Friction velocity
u_m	Bulk velocity
u^+	Dimensionless velocity
X, Y, Z	Coordinates
Greeks	
ρ	Fluid density
ν	Fluid kinematic viscosity
μ	Fluid dynamic viscosity
τ_w	Shear force
λ	Fluid thermal conductivity
η	Comprehensive performance coefficient

1. INTRODUCTION

Turbulence is one of the most common flow patterns in nature, industry and everyday life and most of them appears in the form of wall turbulence. Flow and heat transfer in turbulent boundary layer have attracted widespread attentions.

The generation, maintenance and instability of the turbulence are closely related to the turbulence coherent structure [1], which also plays a significant role in heat transfer and momentum transfer [2]. The speed streaks, burst, and quasi-streamwise vortices are three typical turbulence coherent structure and exist mainly in the viscous sublayer and the buffer layer [3, 4]. The turbulent flow drag reduction and the enhancement of heat transfer can be achieved by controlling the turbulence coherent structure.

This is a paper for the 16th International Conference on Applied Energy (ICAE2024), Sep. 1-5, 2024, Niigata, Japan.

Webb [5] classifies the flow control methods into active and passive categories. The active means need consume external energy, such as electric energy [6], electromagnetic energy [7] , and mechanical vibration [8]. While the common passive control methods are grooving [9], flow-induced vibration [10], vortex generator and so on. In addition, the installation of ribs in the channel can effectively control the flow and heat transfer [11].

Walsh et al. [12-14] found that the longitudinal V-groove riblets with specific dimensionless parameters can achieve the maximum net drag reduction rate of 8%. Zhang et al. [15] found the micro-V-shaped riblet and dimples hybrid surface structure can enhance the heat transfer performance remarkably. Wang et al. [16]combined the fan-shaped grooves and triangular truncated ribs (TRI). When the pumping power was 0.03424, the Nusselt number performance factors reached the maximum 1.081. The mechanism of the heat transfer enhancement was that the intensity of the flow mixing increased and the boundary layer was destroyed.

In addition, Liu et al. [17] arranged the ribs with different truncation modes and arrangement in the high aspect ratio channel (4:1). The generation of the spanwise vortices and reduction of self-sustaining process [18] were the primarily mechanism to optimize heat transfer performance. The truncated ribs can reduce the friction loss without deteriorating the heat transfer as expense in the tested channels. Wang et al. [19] arranged miniature ribs (MRs) in a rectangle channel. The MRs restrain the momentum transfer between the speed streaks and adjust the surrounding vortex distributions. The drag reduction rate in the channel with MRs increased by 17.19%. However, the heat transfer performance decreased. Zheng et al. [20] found that the rids arranged by hierarchical schemes reduced the friction loss but produced slight heat transfer deterioration. Kaewchoothong [21] denoted that the heat transfer performance of the wavy-winglet ribs improved 9.8%-32% than other kinds of ribs. However, the improvement of the heat transfer was accompanied by the high-pressure loss.

In conclusion, the drag reduction and heat transfer enhancement rarely can achieve simultaneously by arranging the ribs in the channel in the previous studies.

However, it is worth noting that the turbulence coherent structures in mainly appear in the velocity boundary layer at $20 < y^+ < 60$ [22]. In addition, the temperature boundary layer and velocity boundary layer in the near-wall region have similar distribution, but the scale is different. As the air is the working fluid, the thickness of the temperature boundary layer is higher than it of the velocity boundary layer[23]. In the present study, the streamwise ribs is arranged in the buffer layer without touching the viscous sublayer in a rectangular channel, which attempt to achieve the drag reduction and maintain the heat transfer performance on the bottom of the channel. The paper adopts the skin friction coefficient, the Nusselt number and the comprehensive performance coefficient to evaluate the drag reduction efficiency and heat transfer enhancement for the channel with ribs at *Re* =3745, 4745, 5745.

2. PHYSICAL MODEL AND NUMERICAL METHOD

2.1 Model details

The calculation domain adopted in the present study is a rectangular channel with dimensions of 4πH×2H×2πH as illustrated in Fig. 1(a). X, Y, Z indicates the streamwise, normal and spanwise direction, respectively and the coordinate origin is situated at the center of bottom edge of the inlet. *u*, *v* and *w* correspond to the fluid velocity component in three directions. H is the half height of the channel.

The definition of the dimensionless parameters adopted in the present study are described as follows:

$$Re = \frac{u_m H}{\nu} \tag{1}$$

where u_m is the bulk velocity, ν indicates the bulk mean kinematic viscosity.

$$y^+ = \frac{y u_\tau}{\nu} \tag{2}$$

$$z^+ = \frac{z u_\tau}{\nu} \tag{3}$$

$$u^+ = \frac{u}{u_\tau} \tag{4}$$

$$u_\tau = \sqrt{\frac{\tau_w}{\rho}} \tag{5}$$

$$\tau_w = \mu \left.\frac{\partial u}{\partial y}\right|_{y=0} \tag{6}$$

$$C_f = \frac{\tau_w}{\frac{1}{2}\rho u_m^{\,2}} \tag{7}$$

where y^+, z^+ are the dimensionless height and dimensionless spanwise width. *y* represents the normal height from the bottom of the channel. *z* is the spanwise

distance. u^+, u_τ denotes the dimensionless velocity and the friction velocity, respectively. τ_w is the spacing-time-averaged wall shear stress. ρ is the density of the fluid and μ is the dynamic viscosity of the fluid. C_f represents the skin friction coefficient.

The channel without passive control is marked as Case 0, while the channel with streamwise ribs is denoted as Case A. The space between each rib is z^+=120. The numerical investigation select three Reynolds number, i. e. 3745, 4745, and 5745. The spacing and number of ribs under different Reynolds numbers will be adjusted and Fig. 1(b) shows the specific arrangement of ribs. The distance between the bottom of ribs and the bottom of the channel is 0.03H. The height of the ribs is 0.1H. This size and arrangement form of the ribs can ensure the ribs do not touch the viscous sublayer and completely immerse in the buffer layer. Meanwhile, in present work, the air is selected as the working fluid. The Prandtl number *Pr* of the air is less than 1, thus the temperature boundary layer is thicker than the velocity boundary layer. The ribs are also situated in the thermal boundary layer completely.

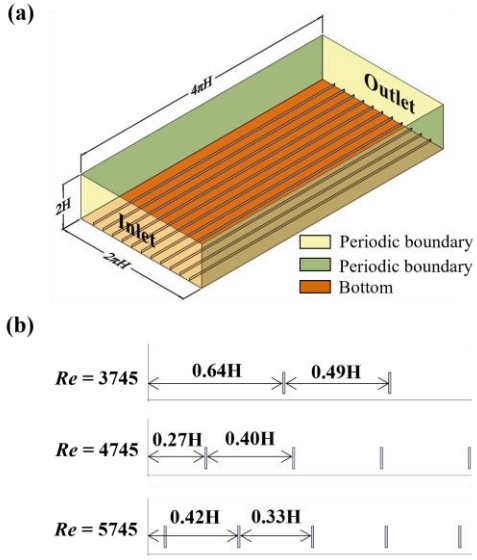

Fig. 1 Schematic diagram of 3D model (a) Overall modelling structure of the Case A channel (b)Details of rib arrangement under different Re

2.2 Governing equations and numerical method

The fluid flows into the computational domain at velocity u_{in} and temperature T_{in}. LES is adopted to solve the governing equations. The continuity equation and Navier-Stokes equations are processed by filter functions. The filtered continuity, momentum and energy equations are expressed as follows:

$$\frac{\partial \overline{u}_i}{\partial x_i}=0 \tag{8}$$

$$\frac{\partial \overline{u}_i}{\partial t}+\frac{\partial \overline{u}_i\overline{u}_j}{\partial x_j}=-\frac{1}{\rho}\frac{\partial \overline{p}}{\partial x_i}+\nu\frac{\partial^2 \overline{u}_i}{\partial x_i\partial x_j}+\frac{\partial \overline{\tau}_{ij}}{\partial x_j} \tag{9}$$

$$\frac{\partial \overline{T}}{\partial t}+\frac{\partial \overline{u}_i\overline{T}}{\partial x_i}=a\frac{\partial^2 \overline{T}}{\partial x_j\partial x_j}+\frac{\partial \overline{q}_j}{\partial x_j} \tag{10}$$

$$\overline{S}_{ij}=\frac{1}{2}\left(\frac{\partial \overline{u}_i}{\partial x_j}+\frac{\partial \overline{u}_j}{\partial x_i}\right) \tag{11}$$

$$\overline{\tau}_{ij}=\overline{u}_i\overline{u}_j-\overline{u_iu_j} \tag{12}$$

where the overbar "-" represents the filtered spatial variables, $\overline{u}_i$ and $\overline{u}_j$ indicate the filtered velocity component, $\overline{T}$ denotes the temperature of the fluid and a means the thermal diffusivity coefficient of the fluid, $\overline{p}$ is the pressure, $\overline{S}_{ij}$ is the rate-of-strain tensor, $\overline{q}_j=\overline{u}_j\overline{T}-\overline{u_jT}$ denotes the sub-grid heat fluxes and $\overline{\tau}_{ij}$ is the anisotropic part of the sub-grid Reynolds stresses.

In order to reflect the influence of sub-grid on LES, it needs to model the sub-grid Reynolds stresses and heat fluxes. Smagorinksy-Lily sub-grid stress (SGS) model [24] is one of the modeling approaches. The modeled sublattice stresses can be described as:

$$\overline{\tau}_{ij}=2\upsilon_t\overline{S}_{ij}+\frac{1}{3}\delta_{ij}\overline{\tau}_{kk} \tag{13}$$

$$\frac{\partial \overline{u}_i}{\partial t}+\frac{\partial \overline{u}_i\overline{u}_j}{\partial x_j}=-\frac{1}{\rho}\frac{\partial \overline{p}}{\partial x_i}+2\frac{\partial\left[\left(\upsilon+\upsilon_t\right)\overline{S}_{ij}\right]}{\partial x_j} \tag{14}$$

$$\overline{P}=\overline{p}+\frac{1}{3}\tau_{ij} \tag{15}$$

$$\upsilon_t=\rho\left(C_s\overline{\Delta}\right)^2S \tag{16}$$

$$S=\left(2\overline{S}_{ij}\overline{S}_{ij}\right)^{\frac{1}{2}} \tag{17}$$

$$\Delta=\left(\Delta x\Delta y\Delta z\right)^{\frac{1}{3}} \tag{18}$$

where v_t represents the sub-grid scale turbulent viscosity. C_s is the Smargorinsky constant which is connected with flow type. For isotropic turbulence, C_s = 0.18, and for fluid near the wall, C_s =0.1. However, according to the actual application, the Smargorinsky constant C_s should be modified as:

$$C_s=0.18\left[1-\exp\left(-\frac{y^+}{A^+}\right)\right] \tag{19}$$

where A^+ represents the semi-empirical constant, respectively.

2.3 Boundary conditions

The numerical simulation boundary conditions are as follows:

(1) Periodic boundary conditions are applied in streamwise and spanwise directions;

(2) No-slip boundary condition are adopted to all walls of the computational domain:

$$u=v=w=0$$

(3) The inlet temperature T_{in} = 300K and the bottom wall temperature T_w = 343K;

(4) the surface of ribs and the top wall of the channel are adiabatic:

$$\frac{\partial T}{\partial x}=\frac{\partial T}{\partial y}=\frac{\partial T}{\partial z}=0$$

2.4 Meshing and sensitivity test

In the present study, the finite volume method and Semi-Implicit Method for Pressure Linked Equations are adopted to solve the Eq. (8)- Eq. (10). The convergence residual is set to 10^{-6} to ensure the accuracy of the numerical calculation.

The computational mesh is generated by a structured hexahedral cell. The details of the mesh is shown in Fig. 2. In order to capture the coherent structure of turbulent boundary layer exactly, mesh refinement is carried out in the boundary layer region around the ribs and the bottom of the channel. The dimensionless height of the first layer of the mesh y^+<1.

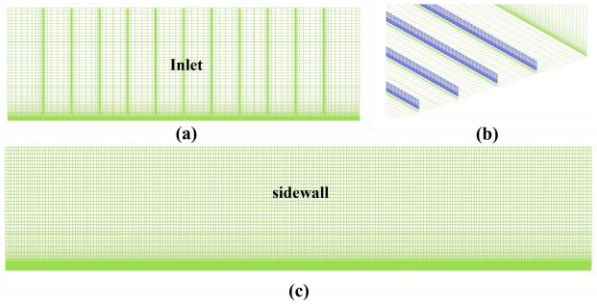

Fig. 2 Schematic diagram of the mesh (a) mesh of the inlet section (b) mesh near the ribs (c) mesh of the side wall surface

As shown in Table 1, five grids are used to verify mesh independency for Case A. Comparing time-averaged Nusselt number and the skin friction coefficient of the bottom of the channel of each grid, the results of Mesh 4 are almost the same as Mesh 5 as shown in Fig. 3.

Table 1 The grid independence verification for Case A

Mesh	$X \times Y \times Z$	Total Cells ($\times 10^6$)
Mesh 1	220 × 60 × 168	2.22
Mesh 2	240 × 60 × 180	2.59
Mesh 3	260 × 60 × 192	3.10
Mesh 4	270 × 70 × 192	3.63
Mesh 5	300 × 80 × 192	4.61

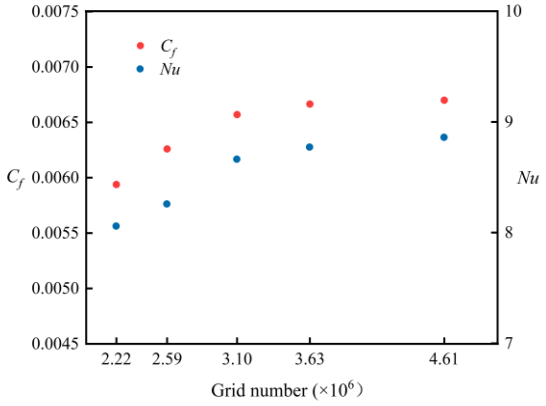

Fig. 3 Nusselt number and the skin friction coefficient for different grids

2.5 Numerical method verification

To verify the accuracy of the present numerical method, the dimensionless velocity distribution in the present study is compared with the experimental result by Durst et al. [25] and DNS results by Kim et al. [26]. As shown in Fi g. 4(a)-(c), the results certify the reliability of the turbulent-velocity field. Fig. 4(d) demonstrates the dimensionless temperature distribution in the different y^+ in the present study and the results by Teitel et al. [27]. The deviation is within the acceptable range.

In conclusion, the results are in good agreement with previous studies, proving the reliability and accuracy of the present numerical method.

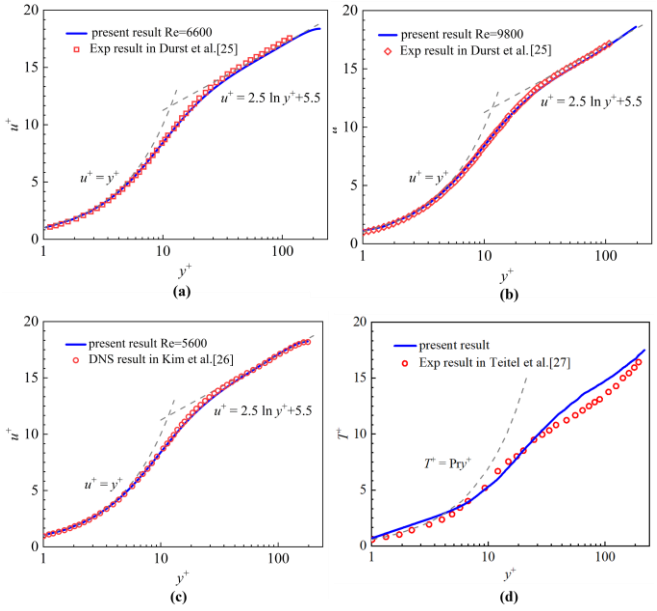

Fig. 4 Validation of code (a) present result and experimental results at Re = 6600 (b) present result and experimental results at Re = 9800 (c) present result and DNS results at Re = 5600 (d) C_f of the present simulation and experimental correlation

3. RESULT AND DISCUSSION

To save space, the characteristics of the flow structure and heat transfer at *Re* = 3745 are investigated as following.

3.1 The flow structures

Firstly, Fig. 5 illustrates the comparison between the flow velocity *u* of the Case 0 and Case A at different y^+. The section of $y^+ = 2$ is located in the viscous sublayer. Due to the limitation of the streamwise ribs, the alternating arrangement of low-speed and high-speed streaks in the viscous sublayer is more regular than that in Case 0, and the range of low-speed streaks spreads out. It can be proved that the overhanging arrangement of the streamwise ribs causes no damage to the viscous sublayer of the turbulent boundary layer. Meanwhile, the regular arrangement of the speed streaks is contributed to stabilize the viscous sublayer and impedes the sweep events of the mainstream high-speed fluid to the viscous bottom layer. At $y^+ = 5$, the section lies between the viscous sublayer and the buffer layer. The ribs restrict the extension of the velocity streaks in spanwise direction. The section of $y^+ = 18.8$ denotes that the ribs have significant constraint effect on streamwise speed streaks in the buffer layer. The section at $y^+ = 100$ in the logarithmic region has a certain normal distance with the ribs. Compared with Case 0, the ribs can reduce the fluid speed in the logarithmic region.

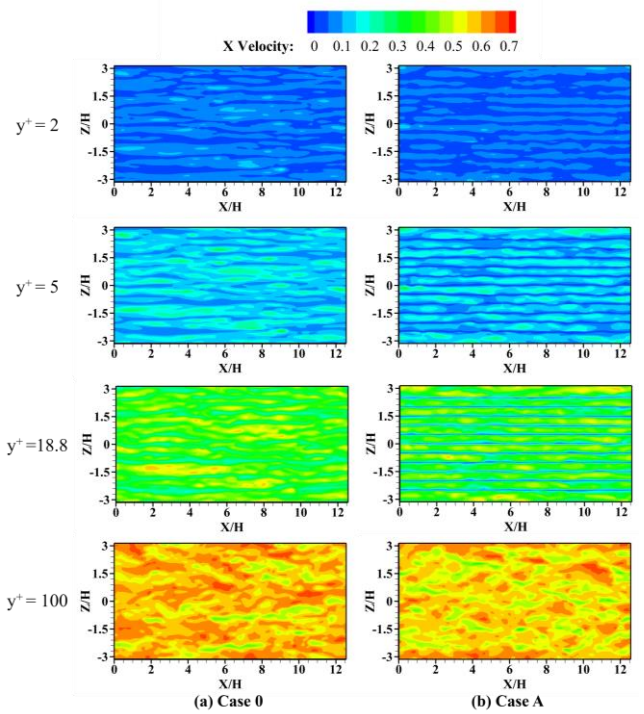

Fig. 5 The flow velocity distribution at different y^+ (a) Case 0 (b) Case A

The Q criterion is used to identify the generation and development of the streamwise vortices on the bottom of the channel in detail. Fig. 6 shows the vortex structure near the bottom of the channel for Case 0 and Case A. Compared with Case 0, the ribs induces the formation of plenty of small-scale streamwise secondary vortices in the buffer layer and the viscous sublayer, thus weakening the turbulence intensity in the channel. These vortices distribute mainly on both sides of the ribs.

In Fig. 6(c), it can be observed more intuitively that the ribs prompt the appearance of the multiple low-speed and small-scale secondary vortices in the viscous sublayer. These newborn vortices move upward to the main stream, and impede the contact between the large-scale streamwise vortices and the bottom of the channel. Meanwhile, the streamwise secondary vortices induced by the ribs in the buffer layer results in the decrease of the spanwise speed above the ribs, while the vortices in the viscous sublayer can move freely in spanwise so as to promote the mixing of the thermal boundary layer. In conclusion, the addition of the ribs can reduce the resistance and maintain the heat transfer capability on the bottom of the channel.

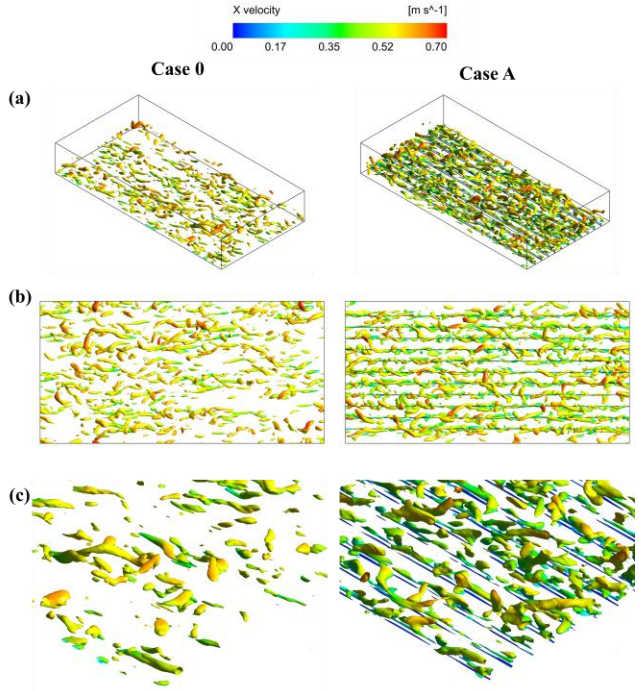

Fig. 6 Vorticity iso-surface defined by Q criterion. (a) 3D vorticity iso-surface defined by Q = 20s^{-1} (b) the top view of 3D vorticity iso-surface defined by Q = 20s^{-1} (c) the zoomed-in view of 3D vorticity iso-surface defined by Q = 30s^{-1}

3.2 Flow and heat transfer characteristics

Comparing the wall shear stress near the wall for Case 0 and Case A in Fig. 7, the wall shear stress

decreases generally in Case A. The drag reduction effect in the region between two ribs is not obvious. However, the ribs to limit the sweep motions accompanied by large-scale vortices, which is the main reason for drag reduction on the bottom. The local wall shear stresses below the ribs are almost zero.

The dimensionless velocity u^+ at different heights for Case 0 and Case A are illustrated in Fig. 8. The secondary vortices induced by the ribs greatly reduces the frequency of the sweep motions so that the u^+ near the wall generally decreases. While $y^+ > 60$, the u^+ in case A is higher than it in Case 0. The reason is that the ribs thicken the velocity boundary layer. At the same y^+, the u_τ in Case A is lower than it in Case 0 so that the u^+ in the logarithmic region increases.

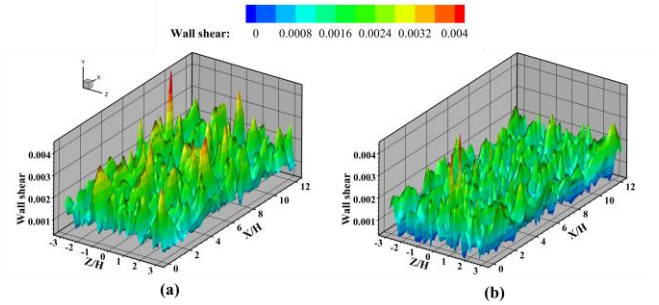

Fig. 7 The wall shear stress distribution on the bottom of the channel at Re =3745 (a) Case 0 (b) Case A

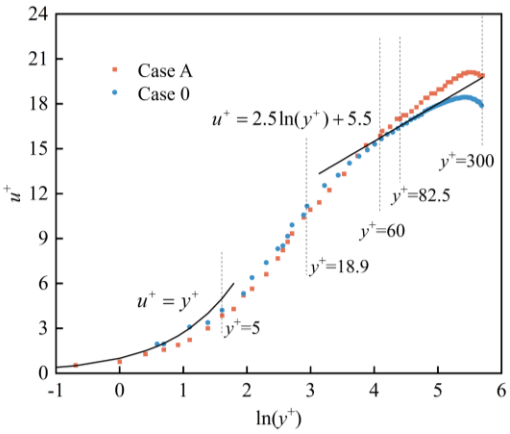

Fig. 8 The u^+ distribution at different y^+ in the channel

The local Nusselt number:

$$Nu_x = \frac{h_x H}{\lambda} \tag{20}$$

The local convection heat transfer coefficient:

$$h_x = \frac{\lambda}{\Delta T}\left.\frac{\partial T}{\partial y}\right|_{y=0} \tag{21}$$

The space-time-averaged results of Nusselt number：

$$Nu = \frac{1}{\tau}\frac{1}{A}\int_0^\tau\int_A Nu_x dA d\tau \tag{22}$$

The streamwise ribs makes the Nusselt number distribution on the bottom regularly in spanwise. The secondary vortices on both sides of the rids limits the sweep motion of the vortices so that the thermal boundary layer below the ribs is undamaged and Nu_x slightly decreases, as shown in Fig. 9(b). While the enough space between adjacent ribs guarantees the sufficient interaction between the main stream and the low-speed fluid near the wall. The Nu_x in these region increases.

The dimensionless temperature T^+ near the wall is defined as:

$$T_\tau = \frac{q_w}{\rho c_p u_\tau} \tag{23}$$

$$T^+ = \frac{\Delta T}{T_\tau} \tag{24}$$

where T_τ represents the wall friction temperature and q_w is the wall heat flux.

As shown in Fig. 10, the global distribution of the T^+ at different y^+ in Case A is almost no different from that in Case 0. Comparing with Case 0, the T^+ in Case A slightly decreases in the viscous sublayer and slightly increases in the buffer layer. The secondary vortices in the buffer layer enhance the heat convection, which is the other approach to compensate for the decreasing heat transfer below the ribs.

In summary, at *Re* = 3745, for the entire bottom of the channel, the heat transfer performance has not been significantly impacted.

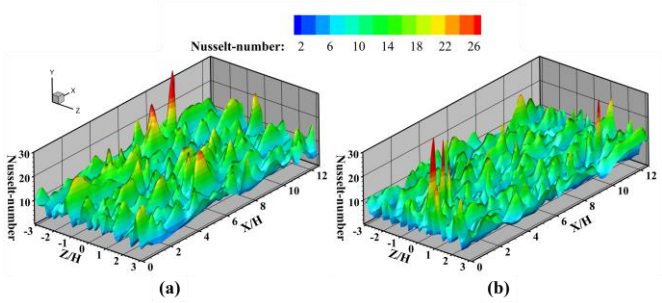

Fig. 9 The Nusselt number distribution on the bottom surface of the channel at Re =3745 (a) Case 0 (b) Case A

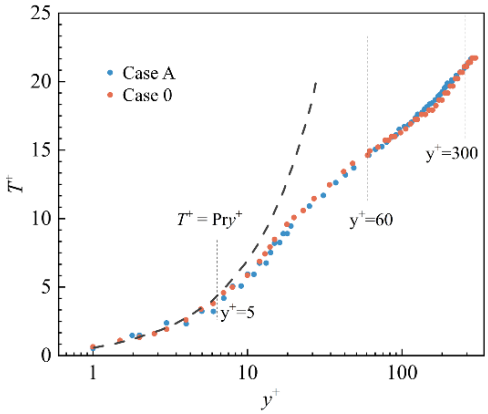

Fig.10 The T^+ distribution at different y^+ in the channel

3.3 Comprehensive performance evaluation

The comprehensive performance coefficient η is used to evaluate the flow and heat transfer performance in the channel, denoted as:

$$\eta = \frac{Nu / Nu_0}{(C_f / C_{f0})^{1/3}} \tag{25}$$

At *Re* = 3745, the *Nu* decreases slightly while the average skin friction coefficient decreases by 12.879%. At *Re* = 4745, 5745, the average C_f dramatically decreases by 16.481% and 26.282%, while the heat transfer performance is not deteriorated but enhanced slightly. As the Re increases, the ribs are also completely included at $20 < y^+ < 60$. Therefore, the control effects of the ribs on flow coherence structure in turbulent flow boundary layer is better, thus the reduction of resistance is more significant at higher Re. The ribs immersed in the thermal boundary layer can improve the heat convection in the buffer layer, which makes the thermal performance of the channel maintains basically at the slightly higher level.

Table 2 The Nusselt number, skin friction coefficient and comprehensive performance coefficient for Case 0 and Case A at different Re.

Re	Case	*Nu*	C_f	η
3745	Case 0	8.942	0.00783	1
	Case A	8.773 (↓1.887%)	0.00666 (↓12.879%)	1.035
4745	Case 0	10.674	0.00729	1
	Case A	11.151 (↑0.45%)	0.00609 (↓16.481%)	1.109
5745	Case 0	12.677	0.00702	1
	Case A	12.736 (↑0.46%)	0.00518 (↓26.282%)	1.112

4. CONCLUSIONS

In this paper, the flow and heat transfer characteristics in the channel with the streamwise ribs arranged in the buffer layer are analyzed. With the *Re* = 3745, 4745 and 5745, the velocity streaks, flow vortex structure, Nusselt number, wall friction coefficient and the comprehensive performance coefficient in the channel are investigated. Based on the numerical results, the following conclusions are obtained:

1. The arrangement of streamwise ribs makes the distribution of the high and low speed streaks in the viscous sublayer and the buffer layer is very regular.
2. The ribs induce many small-scale secondary vortex structures in the viscous bottom layer and the buffer layer. The secondary vortices limit the sweeping motion on the wall of the high-speed fluid carried by the large-scale vortex structure, and restrain the spanwise motion of the large-scale vortex. The reduction effect of the resistance on bottom of the channel is significant.
3. The sweep motions occurring between the adjacent ribs can destroy the thermal boundary layer and ensure the heat transfer near the wall. The excess heat transfer compensates the local heat loss below the ribs.
4. The streamwise ribs arranged in the buffer layer can attain a good drag reduction effect on the bottom of the channel without affecting the heat transfer. When the *Re* = 3745, 4745 and 5745, the comprehensive performance coefficients η gradually increase.

This method of arranging the streamwise riblets in the buffer layer has outstanding drag reduction effect without sacrificing the heat transfer capacity of the bottom of the channel. In practical engineering, this device can reduce energy consumption.

REFERENCE

[1] Praturi AK, Brodkey RS. A stereoscopic visual study of coherent structures in turbulent shear flow. Journal of Fluid Mechanics. 1978;89:251-72.

[2] Adrian RJ. Hairpin vortex organization in wall turbulencea). Physics of Fluids. 2007;19:041301.

[3] Marusic I, McKeon BJ, Monkewitz PA, Nagib HM, Smits AJ, Sreenivasan KR. Wall-bounded turbulent flows at high Reynolds numbers: Recent advances and key issues. Physics of Fluids. 2010;22:065103.

[4] Robinson SK. Coherent Motions in the Turbulent Boundary Layer. Annual Review of Fluid Mechanics. 1991;23:601-39.

[5] Webb RL. Principles of Enhanced Heat Transfer. 1994.

[6] Zhang J, Luo X, Wang L, Feng Z, Li T. Combined effect of electric field and nanofluid on bubble behaviors and heat transfer in flow boiling of minichannels. Powder Technology. 2022;408:117743.

[7] Zhang X, Huang H. Effect of magnetic obstacle on fluid flow and heat transfer in a rectangular duct. International Communications in Heat and Mass Transfer. 2014;51:31-8.

[8] Fu J, Miao X, Zuo Q, Tang H, Li Y, Zhang Y, et al. Heat transfer and field synergy characteristics in a rectangular unit channel under mechanical vibration. International Communications in Heat and Mass Transfer. 2022;136:106176.

[9] Choi H, Moin P, Kim J. Direct numerical simulation of turbulent flow over riblets. Journal of Fluid Mechanics. 1993;255:503-39.

[10] Duan D, Ge P, Bi W. Numerical investigation on heat transfer performance of planar elastic tube bundle by flow-induced vibration in heat exchanger. International Journal of Heat and Mass Transfer. 2016;103:868-78.
[11] Soleimani S, Eckels S. A review of drag reduction and heat transfer enhancement by riblet surfaces in closed and open channel flow. International Journal of Thermofluids. 2021;9:100053.
[12] Walsh M. Turbulent boundary layer drag reduction using riblets. 20th Aerospace Sciences Meeting: American Institute of Aeronautics and Astronautics; 1982.
[13] Walsh M, Lindemann A. Optimization and application of riblets for turbulent drag reduction. 22nd Aerospace Sciences Meeting: American Institute of Aeronautics and Astronautics; 1984.
[14] Walsh MJ. Riblets as a Viscous Drag Reduction Technique. AIAA Journal. 1983;21:485-6.
[15] Zhang P, Rao Y, Xie Y, Zhang M. Turbulent flow structure and heat transfer mechanisms over surface vortex structures of micro V-shaped ribs and dimples. International Journal of Heat and Mass Transfer. 2021;178:121611.
[16] Wang QH, Tao JY, Cui Z, Zhang TT, Chen GY. Numerical simulation of fluid and heat transfer characteristics of microchannel heat sink with fan-shaped grooves and triangular truncated ribs. International Communications in Heat and Mass Transfer. 2024;155.
[17] Liu J, Hussain S, Wang J, Wang L, Xie G, Sundén B. Heat transfer enhancement and turbulent flow in a high aspect ratio channel (4:1) with ribs of various truncation types and arrangements. International Journal of Thermal Sciences. 2018;123:99-116.
[18] Smits AJ, Delo C. Self-Sustaining Mechanisms of Wall Turbulence. 2001.
[19] Wang JS, Yang ZQ. The Characteristics of Heat Transfer and Flow on a Surface with Small Scale V-Shape Groove. Proceedings of the Asme Micro/Nanoscale Heat and Mass Transfer International Conference, Vol 3. 2010:137-42.
[20] Zheng SF, Liu GQ, Zhang Y, Wang HC, Gao SR, Yang YR, et al. Performance evaluation with turbulent flow and heat transfer characteristics in rectangular cooling channels with various novel hierarchical rib schemes. International Journal of Heat and Mass Transfer. 2023;214.
[21] Kaewchoothong N, Nuntadusit C, Gonsrang S, Luengchavanon M, Chatpun S. Numerical Study on Flow Field and Heat Transfer Enhancement in a Cooling Channel With Novel Ribs Based on Battery Thermal Management System. Heat Transfer Eng. 2024.
[22] Hamilton JM, Kim J, Waleffe F. Regeneration mechanisms of near-wall turbulence structures. Journal of Fluid Mechanics. 1995;287:317-48.
[23] Snijders AL, Koppius AM, Nieuwvelt C. An experimental determination of the turbulent prandtl number in the inner boundary layer for air flow over a flat plate. International Journal of Heat and Mass Transfer. 1983;26:425-31.
[24] Meneveau C, Katz J. Scale-Invariance and Turbulence Models for Large-Eddy Simulation. Annual Review of Fluid Mechanics. 2000;32:1-32.
[25] Durst F, Kikura H, Lekakis I, Jovanović J, Ye Q. Wall shear stress determination from near-wall mean velocity data in turbulent pipe and channel flows. Experiments in Fluids. 1996;20:417-28.
[26] Kim J, Moin P, Moser R. Turbulence statistics in fully developed channel flow at low Reynolds number. Journal of Fluid Mechanics. 1987;177:133-66.
[27] Teitel M, Antonia RA. Heat transfer in fully developed turbulent channel flow: comparison between experiment and direct numerical simulations. International Journal of Heat and Mass Transfer. 1993;36:1701-6.